Unsteady propagation of a liquid plug in a liquid-lined straight tube

Hideki Fujioka, Shuichi Takayama, and James B. Grotberg
Biomedical Engineering Department, University of Michigan, Ann Arbor, Michigan 48109, USA

(Received 13 December 2007; accepted 12 May 2008; published online 24 June 2008)

This paper considers the propagation of a liquid plug driven by a constant pressure within a rigid axisymmetric tube whose inner surface is coated by a thin liquid film. The Navier–Stokes equations are solved using the finite-volume method and the SIMPLEST algorithm. The effects of precursor film thickness, initial plug length, pressure drop across the plug, and constant surface tension on the plug behavior and tube wall mechanical stresses are investigated. As a plug propagates through a liquid-lined tube, the plug gains liquid from the leading front film, and it deposits liquid into the trailing film. If the trailing film is thicker (thinner) than the precursor film, the plug volume decreases (increases) as it propagates. For a decreasing volume, eventually the plug ruptures. Under a specific set of conditions, the trailing film thickness equals the precursor film thickness, which leads to steady state results. The plug speed decreases as the precursor film thins because the resistance to the moving front meniscus increases. As the pressure drop across the plug decreases, the plug speed decreases resulting in thinning of the trailing film. As the plug length becomes longer, the viscous resistance in the plug core region increases, which slows the plug and causes the trailing film to become even thinner. The magnitude of the pressure and shear stress at the tube inner wall is maximum in the front meniscus region, and it increases with a thinner precursor film. As the surface tension increases, the plug propagation speed decreases, the strength of the wall pressure in the front meniscus region increases, and the pressure gradient around the peak pressure becomes steeper. © *2008 American Institute of Physics*. [DOI: 10.1063/1.2938381]

I. INTRODUCTION

Liquid plugs form in pulmonary airways due to both internal and external liquid sources. Internally, the inner airway surfaces of the lung are covered by a thin liquid layer. This liquid layer is unstable and forms a plug due to a capillary instability[1–3] if the film thickness is sufficiently large. When lung-surfactant availability is reduced, this tendency to form liquid plugs can be increased.[4] This occurs particularly near the end of expiration in distal airways, causing the airways to close due to plug formation. Once formed, the liquid plug propagates driven by inhaled air and can rupture under certain conditions or persist under others. During the airway-reopening process, pulmonary epithelial cells may be damaged by mechanical stresses associated with fluid motion[5,6] and plug rupture.[7]

Externally, liquid is instilled into the pulmonary airways in some medical treatments such as surfactant replacement therapy (SRT),[8–12] partial liquid ventilation (PLV),[13–19] and drug delivery.[20–29] The formation of a liquid plug in the trachea, before inspiration, is important in creating a more uniform liquid distribution throughout the lung.[30]

Bilek *et al.*[5] investigated surface-tension-induced lung epithelial cell damage in a model of airway reopening, consisting of a semi-infinite bubble (air finger) propagating in a narrow fluid-filled channel lined with pulmonary epithelial cells. They showed that cell damage increased with decreasing reopening velocity and that the presence of pulmonary surfactant prevented this injury. Based on a computational model, they concluded that the steep pressure gradient near the finger front was the most likely cause of the observed cellular damage. Kay *et al.*[6] showed that cell damage was directly correlated with the pressure gradient, not the duration of stress exposure (period for a pressure wave to pass over a cell). Repeated reopening and closure caused the cell layer to be damaged, even under conditions that would not lead to extensive damage from a single reopening event.

Huh *et al.*[7] investigated mechanical injury of primary human small airway epithelial cells (SAECs) caused by reopening stresses and respiratory crackles in compartmentalized microfluidic systems that can produce polarized and differentiated small airway epithelium *in vitro*. The microfluidic channel was lined with SAECs and a thin liquid film. Dynamic propagation and rupture of liquid plugs through the channel were generated by a microfluidic component. Exposure of the SAECs to physiological fluid mechanical stresses associated with surfactant-deficient airway reopening led to significant cellular damage whose severity was elevated with increasing frequency of plug propagation and rupture. Furthermore, plug rupture that generates explosive pressure and shear stress waves imposed a higher risk of cellular injury than plug propagation alone.

Most theoretical studies on plug propagation in liquid-lined channels or tubes, with or without surfactant, have been carried out in the Stokes flow regime, neglecting the effects of fluid inertia, that is, in the limit of zero Reynolds number. Howell *et al.*[31] analyzed surfactant-free liquid plug propagation in a prewetted flexible tube in the asymptotic limit of $\mathrm{Ca} \to 0$, where $\mathrm{Ca} = \mu U / \sigma$ is the capillary number, μ is the fluid viscosity, σ is the surface tension, and U is the fluid speed. Since the viscous dissipation in the plug core region is negligibly small as $\mathrm{Ca} \to 0$, they assumed a uniform pressure

in the plug core. They identified a critical imposed pressure drop above which the liquid plug would eventually rupture. Waters and Grotberg[32] asymptotically investigated the effects of soluble surfactant on liquid plug propagation. They showed that the driving pressure difference ΔP for a given Ca increased with increasing surface elasticity but decreased with the precursor film thickness. The trailing film thickness increased with ΔP, but at a slower rate when the surface elasticity was large.

Fujioka and Grotberg[33] numerically investigated steady propagation of a liquid plug with a surfactant-free interface. They showed that the trailing film thickness decreased as the plug length decreases below the channel width. A capillary wave developed in the precursor film near the front meniscus as the Reynolds number increases. In this region, both wall pressure and shear stress have sharp peaks in the capillary wave located at the front interface. Particularly, with finite Reynolds number, these peak stresses are significantly larger than those at the rear. In addition, the single finger of air has a trailing film, which increases in thickness as Ca increases. Therefore, as the finger speed increases, the thickening trailing film moderates the increase of the wall shear stress in the transition region. These facts suggest that there is a higher risk of pulmonary epithelial cell damage in the front of the liquid plug than in the rear.

Subsequently, Fujioka and Grotberg numerically investigated the effect of surfactant on the steady propagation of a liquid plug within a two-dimensional channel.[34] The Marangoni stress due to the gradient in the surface tension rigidifies the interface, which causes the precursor film thickness near the meniscus to be thicker than the leading film thickness and reduces the peaks of wall pressure and wall shear stress.

In our previous analysis,[33] the precursor film thickness needed to equal the trailing film thickness due to the steady flow limit. Since the wall pressure and shear stress are strongly influenced by the film thickness, it is important to investigate the effect of precursor film thickness on these stresses. In this study, we perform a numerical analysis for time-dependent liquid plug propagation in a tube. The plug is driven by a constant pressure drop between the front and rear air phases. A constant surface tension is assumed. The effects of precursor film thickness, initial plug length, pressure drop, and surface tension on the fluid dynamics of liquid plugs are investigated.

II. METHOD

A. Model description

In this paper, we investigate the propagation of a liquid plug inside a circular rigid tube of radius R, as shown in Fig. 1. A pressure difference between the front and rear air fingers, $\Delta P^* = P_1^* - P_2^*$, drives the liquid plug consisting of an incompressible Newtonian fluid. The gas-phase viscosity is assumed negligible, so only fluid dynamics in the liquid phase is considered. A constant surface tension is assumed. The plug is assumed to be axisymmetric about the center line of the tube, so that all quantities are uniform in the circumferential direction and the circumferential velocity is zero. Dimensionless forms of the Navier–Stokes equations and the continuity equation are

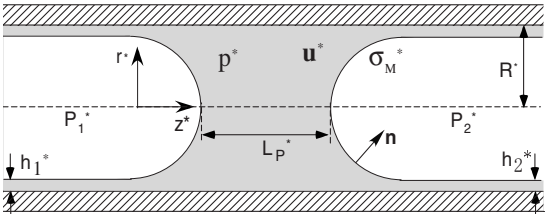

FIG. 1. Liquid plug model.

$$\lambda\left\{\left[\frac{\partial u_z}{\partial t}\right]_{\mathbf{x}} + u_r\frac{\partial u_z}{\partial r} + u_z\frac{\partial u_z}{\partial z}\right\} = -\frac{\partial p}{\partial z} + \frac{1}{r}\frac{\partial}{\partial r}\left(r\frac{\partial u_z}{\partial r}\right) + \frac{\partial^2 u_z}{\partial z^2}, \tag{1}$$

$$\lambda\left\{\left[\frac{\partial u_r}{\partial t}\right]_{\mathbf{x}} + u_r\frac{\partial u_r}{\partial r} + u_z\frac{\partial u_r}{\partial z}\right\} = -\frac{\partial p}{\partial r} + \frac{\partial}{\partial r}\left[\frac{1}{r}\frac{\partial (ru_r)}{\partial r}\right] + \frac{\partial^2 u_r}{\partial z^2}, \tag{2}$$

$$\frac{1}{r}\frac{\partial (ru_r)}{\partial r} + \frac{\partial u_z}{\partial z} = 0, \tag{3}$$

where $\mathbf{u}=(u_z,u_r,0)=\mathbf{u}^*/(\sigma_M/\mu)$ is the dimensionless fluid velocity vector: μ is the liquid viscosity and σ_M is the surface tension of the air-liquid interface. $p=p^*/(\sigma_M/R)$ is the dimensionless pressure, R is the tube radius, $t=t^*/(\mu R/\sigma_M)$ is the time, $z=z^*/R$, and $r=r^*/R$. The dimensionless parameter $\lambda=\rho\sigma_M R/\mu^2$, where $\lambda^{-1/2}$ is called the Ohnesorge number, is determined by only the tube geometry and the properties of the fluid; thus, it characterizes the fluid and tube size. ρ is the liquid density. The subscript $\mathbf{x}$ in the time derivative indicates that the derivative follows a fixed (z,r) point.

The no-slip condition is applied on the tube wall, which is $\mathbf{u}=0$ at $r=1$. For the axisymmetric condition, at the tube center $r=0$, the radial component of the velocity is zero, $u_r=0$, and the gradient of the axial velocity in the r-direction is zero, $\partial u_z/\partial r=0$. At the end boundaries in both the precursor and trailing films, a stationary condition is applied: $\mathbf{u}=0$ and $\partial p/\partial z=0$. At each air-liquid interface, we apply a kinematic boundary condition,

$$(\mathbf{u}-\dot{\mathbf{X}})\cdot\mathbf{n}=0, \tag{4}$$

where $\dot{\mathbf{x}}$ is the velocity of the interface node point and $\mathbf{n}$ is the unit vector normal to the interface. A balance of normal forces which accounts for the jump in stress due to surface tension is

$$-p\mathbf{n}+(\nabla\mathbf{u}+\nabla\mathbf{u}^T)\cdot\mathbf{n}=\kappa\mathbf{n}-P_a\mathbf{n}, \tag{5}$$

where P_a is the air pressure ($a=1$ or 2), $\kappa=\kappa^* R$ is the dimensionless interface curvature, and $\nabla=\mathbf{e}_z(\partial/\partial z)+\mathbf{e}_r(\partial/\partial r)+\mathbf{e}_\theta(\partial/\partial\theta)/r$.

B. Coordinate transformation

The grid nodes were generated using the elliptic generation system[35] where a uniform computational domain (ξ, η) is mapped inside a plug domain (z,r) that is determined by the solution of the two-dimensional Poisson's equations. Local grid adjustment is done to satisfy a local orthogonal grid at the free surface:[36] taking a vertex on the free surface, the local normal direction is taken into the interior and its first intersection with an interior cell face is selected as a new interior vertex. In terms of the transformed variables, the momentum equation is written as

$$\lambda\left[\frac{\partial(J\mathbf{u})}{\partial t}\right]_{\xi} + \frac{\partial}{\partial \xi}\left[\lambda(F^{\xi} - G^{\xi})\mathbf{u} - \frac{B_{11}}{J}\frac{\partial \mathbf{u}}{\partial \xi}\right] + \frac{\partial}{\partial \eta}\left[\lambda(F^{\eta} - G^{\eta})\mathbf{u} - \frac{B_{22}}{J}\frac{\partial \mathbf{u}}{\partial \eta}\right] = \Upsilon, \tag{6}$$

where

$$\mathbf{F} = [F^{\xi} \quad F^{\eta}]^T = \mathbf{A}\mathbf{u}, \tag{7}$$

$$\mathbf{G} = [G^{\xi} \quad G^{\eta}]^T = \mathbf{A}\dot{\mathbf{X}}, \tag{8}$$

$$\mathbf{A} = A_{ij} = r\begin{bmatrix} \dfrac{\partial r}{\partial \eta} & -\dfrac{\partial z}{\partial \eta} \\ -\dfrac{\partial r}{\partial \xi} & \dfrac{\partial z}{\partial \xi} \end{bmatrix}, \quad \mathbf{B} = B_{ij} = \mathbf{A}\mathbf{A}^T, \tag{9}$$

$$\Upsilon = -\mathbf{A}^T\nabla_{\xi} p + \frac{\partial}{\partial \xi}\left(\frac{B_{12}}{J}\frac{\partial \mathbf{u}}{\partial \eta}\right) + \frac{\partial}{\partial \eta}\left(\frac{B_{21}}{J}\frac{\partial \mathbf{u}}{\partial \xi}\right) - J\frac{(\mathbf{u}\cdot\mathbf{e}_r)}{r^2}\mathbf{e}_r, \tag{10}$$

and $\nabla_{\xi} = \mathbf{e}_{\xi}(\partial/\partial\xi) + \mathbf{e}_{\eta}(\partial/\partial\eta)$. Here $\mathbf{A}$ is the transformation matrix that represents the projected area of a control surface normal to the ith axis (representing ξ, η) onto the jth plane (representing z, r). The control volume is $J = r^{-1}|\mathbf{A}|$, the Jacobian of the transformation. The components of $\mathbf{F}$ are the mass flow rates through the control surface normal to the ξ and η axes and are defined as the velocities in the computational space. The primary diffusion terms, which include the B_{ij} $(i=j)$ components, represent the diffusive fluxes through the control surfaces normal to the ξ and η axes. The secondary diffusion terms, which include the B_{ij} $(i \neq j)$ components which are zero if the mesh lines are orthogonal, represent artifacts from the geometric transformation and are treated as source terms in the computational model.

The transformed continuity equation is

$$\nabla_{\xi}\cdot\mathbf{F} = 0. \tag{11}$$

Assuming that the interface corresponds to the η axis, the unit normal on the η axis can then be described by

$$\mathbf{n} = \frac{1}{\sqrt{B_{11}}}\begin{bmatrix} A_{11} \\ A_{12} \end{bmatrix}, \tag{12}$$

and the kinematic boundary condition on the interface (η grid line) [Eq. (4)] is modified to

$$(F^{\xi} - G^{\xi})_S = 0. \tag{13}$$

C. Numerical procedure

The transformed equations [Eqs. (6) and (11)] are solved using the SIMPLEST algorithm (SIMPLE with splitting technique).[37] A kinematic update scheme is employed to update the interface location.[38] The velocity field is computed according to the following algorithm.

(1) The calculation starts from the initial condition described in Sec. II D.
(2) The interface shapes are approximated using cubic splines[39] as functions of the arc length along each interface. The normal and tangential vectors are calculated using the first derivative of the interpolated functions.
(3) Poisson's equations are solved using the SOR (successive over-relaxation method) scheme to generate the grid inside the domain.[35] The geometric quantities such as the transformed matrix can then be calculated.
(4) The grid velocity is computed. In this study, the predicted grid velocity $\mathbf{G}^P$ is defined by

$$\mathbf{G}^P = \mathbf{A}\dot{\mathbf{X}}^P \cong \mathbf{A}_{t_1}[\mathbf{X}^P(\underline{\xi}, t_1) - \mathbf{X}(\underline{\xi}, t_0)]/\Delta t, \tag{14}$$

where t_1 is the current time, t_0 is the previous time, $\Delta t = t_1 - t_0$ is the time step, and $\mathbf{X}^P(\xi, t_1)$ is the grid point at the current time, which is updated during iteration steps.
(5) The pressure is solved using the known temporary mass flux rates $\hat{\mathbf{F}}$, which are computed from the discrete form of the momentum equation without the pressure term. The SUPERLU solver[40] is used to solve the sparse linear system.
(6) The momentum equations are solved using the pressure field p^P obtained in step (5).
(7) The pressure correction equation is solved using the predicted velocity field $\mathbf{F}^P$, which is the solution of the momentum equations obtained in step (6).
(8) The velocity field is corrected by $\mathbf{F}^{PP} = \mathbf{F}^P + \mathbf{F}'$. The correction is determined by the pressure correction values, p', obtained in step (7) as $\mathbf{F}' = -\mathbf{B}\nabla_{\underline{\xi}} p'/a_P$, where a_P is a diagonal element of the linear system matrix for the momentum equations. The fluid velocity on the interface, $F_S^{\xi P}$, is not corrected at this step.
(9) The position of the interface is updated using the kinematic condition [Eq. (13)]. Assuming $\mathbf{G} = \mathbf{G}^P + \mathbf{G}'$ and $\mathbf{F} = \mathbf{F}^P + \mathbf{F}'$, the correction for the grid velocity on the interface is

$$G_S^{\xi'} = F_S^{\xi P} - G_S^{\xi P} + F_S^{\xi'}. \tag{15}$$

The interface grid position is updated by

$$\mathbf{X}(\underline{\xi}_S, t_1) = \mathbf{X}^P(\underline{\xi}_S, t_1) + \mathbf{n}\frac{R_X}{\sqrt{B_{11}}}G^{\xi'}\Delta t, \tag{16}$$

where R_X is an under-relaxation factor, $0 < R_X \leqslant 1$, and $\mathbf{n}$ is a unit normal.

(10) The pressure is solved again using the temporary mass flux rates $\hat{\mathbf{F}}^{PP}$, which are computed using $\mathbf{F}^{PP}$.
(11) The second correction for the velocity field is made by applying $\mathbf{F}^{PPP}=\hat{\mathbf{F}}^{PP}-\mathbf{B}\nabla_{\xi}p^{PPP}/a_P$, where p^{PPP} is the solution in step (10).
(12) Reset $\mathbf{F}^{PPP}\rightarrow\mathbf{F}$, $\mathbf{X}\rightarrow\mathbf{X}^P$. Steps (2)–(11) are repeated until $\mathbf{F}$ and $\mathbf{G}$ converge, which is defined by the differences from the previous iteration satisfying the convergence criteria.[33]
(13) Increment time step and go to step (2).

D. Initial conditions

In this study, the course of liquid plug propagation in an axisymmetric tube is investigated. Initially, a liquid plug of length L_{P0} begins to move by a constant driving pressure, $\Delta P=P_1-P_2$, which is the pressure difference between the front and rear air phases. The plug length L_P is defined as the distance between the front and rear meniscus tips, where the tips are always located at $r=0$ on both interfaces for the axisymmetric plug. The initial plug shape is approximated by a hemisphere of radius $1-h_2$ for front and rear menisci, the length between both meniscus tips L_{P0}, and a uniform film thickness of h_2 on both sides of the plug. The initial liquid velocity is set to be zero uniformly. The precursor and trailing films are extended eight times the tube radius.

E. Dimensionless parameters

The dimensionless parameters are $\lambda=\rho\sigma_M R/\mu^2$, the initial plug length $L_{P0}=L_{P0}^*/R$, the pressure drop across the plug $\Delta P=\Delta P^*/(\sigma_M/R)$, and the precursor film thickness $h_2=h_2^*/R$. Since the properties of Survanta (Ross Labs, Columbus, OH), which is a highly surface-active and biologically derived pulmonary surfactant used in SRT, are $\rho=0.94$ g/cm^3, $\mu=42$ cP, and $\sigma_M=25$ dyn/cm,[41] λ for SRT has a range of $1<\lambda<20$ for airway generations from 0 to 13 in an infant lung. In PLV or airway closure, the values of λ are larger than those in SRT, and inertial effects cannot be neglected. For example, for perfluorocarborn Peflubron (Alliance Pharmaceuticals, San Diego, CA), $\rho=1.93$ g/cm^3, $\mu=2.1$ cP, and $\sigma_M=18$ dyn/cm.[41] Thus, the range of λ is approximately $10^3<\lambda<10^4$. For plugs created by an internal source in a surfactant-reduced lung, assuming $\rho=1$ g/cm^3, $\mu=10$ cP, and $\sigma_M=50$ dyn/cm, λ has a range of $10^2<\lambda<5\times10^3$ for airway generations from 0 to 16 in an adult lung. In the present study, since we focus on a compromised lung, higher surface tension is assumed and hence $\lambda=1000$ is used.

The inspiratory positive airway pressure typically used for conventional mechanical ventilators is approximately 10 cm H_2O. If this pressure acts on one side of a liquid plug in airways ($\Delta P^*\sim10\times980$ dyn/cm^2), the dimensionless pressure drop ΔP is $O(10)$ at the airway of $R\sim0.1$ cm and surface tension of 50 dyn/cm. However, the actual ΔP will be smaller than this value due to pressure dissipation in the upper airways. In this study, for most of the computations, $\Delta P=1$ is used.

The liquid film thickness in the small airways in the lung is approximately 0.02 of the airway radius according to measurements on guinea pig lungs by Yager *et al.*[42] Unhealthy lungs commonly produce excessive bronchial secretions, which increase the film thickness to 0.2 of the airway radius.[43] The precursor film thickness employed in the present study ranges from 0.01 to 0.13, and 0.05 is used as a base value.

According to a linear stability analysis for a thin film that coats the inner surface of a circular tube, the wavelength that maximizes the film growth rate is $2^{3/2}\pi$ of the tube radius. Assuming an airway lined by a liquid film with thickness of 0.1–0.2 of the radius, if a plug forms, the length of the plug will be approximately 1. In this study, the initial plug length, $L_{P0}=1$, is used as a base value.

F. Definition of plug rupture

When a liquid plug propagates, if the mass deposited to the trailing film is greater than the mass gained from the precursor film, the plug becomes shorter and shorter and eventually ruptures. At the time of plug rupture, the front and rear interfaces contact with each other, but the current numerical method cannot resolve this situation. When the interfaces become close, the inner iteration step [see Sec. II C, step (12)] does not converge. In this study, we assume that the plug ruptures at this moment. For the present study, the inner iteration failed when L_P becomes below 5×10^{-3}.

G. Numerical mesh and time step

Since we employ a boundary fitted mesh, the mesh changes as the interface deforms. The grid structure is the same as our previous papers.[33,34] The number of node points is determined based on the previous studies. For the initial plug length $L_{P0}=1$ case, 6201 total node points, 9 node points in film depth, 241 node points on each free surface, and 41 node points between the front and rear menisci tips is employed. The number of node points is fixed during each computation.

A time step of $\Delta t=0.0982$ ($\sim2\pi/64$) is used for all computations and is considered sufficiently small for the present problem since the range of the dimensionless velocity is small (Ca<0.05). We have examined the L_P and Ca behaviors for three different time steps, $\Delta t=2\pi/32$, $2\pi/64$, and $2\pi/128$, for $h_2=0.05$, $\Delta P=1$, $\lambda=1000$, and $L_{P0}=1$. At $t=100$, $L_P=0.852$, 0.858, and 0.860, and Ca=0.0283, 0.0283, and 0.0283; at $t=200$, $L_P=0.524$, 0.554, and 0.558, and Ca=0.0360, 0.0356, and 0.0353; at $t=270$, $L_P=0.230$, 0.279, and 0.281, and Ca=0.0414, 0.0401, and 0.0401, for $\Delta t=2\pi/32$, $2\pi/64$, and $2\pi/128$. The difference between $2\pi/64$ and $2\pi/128$ was insignificant.

III. RESULTS

A. Effect of precursor film thickness

Figure 2 demonstrates how the plug length and speed change as the plug propagates for the various precursor film thicknesses h_2 at $\lambda=1000$ for an initial plug length of $L_{P0}=1$ and other initial conditions, as described in Sec. II D. The

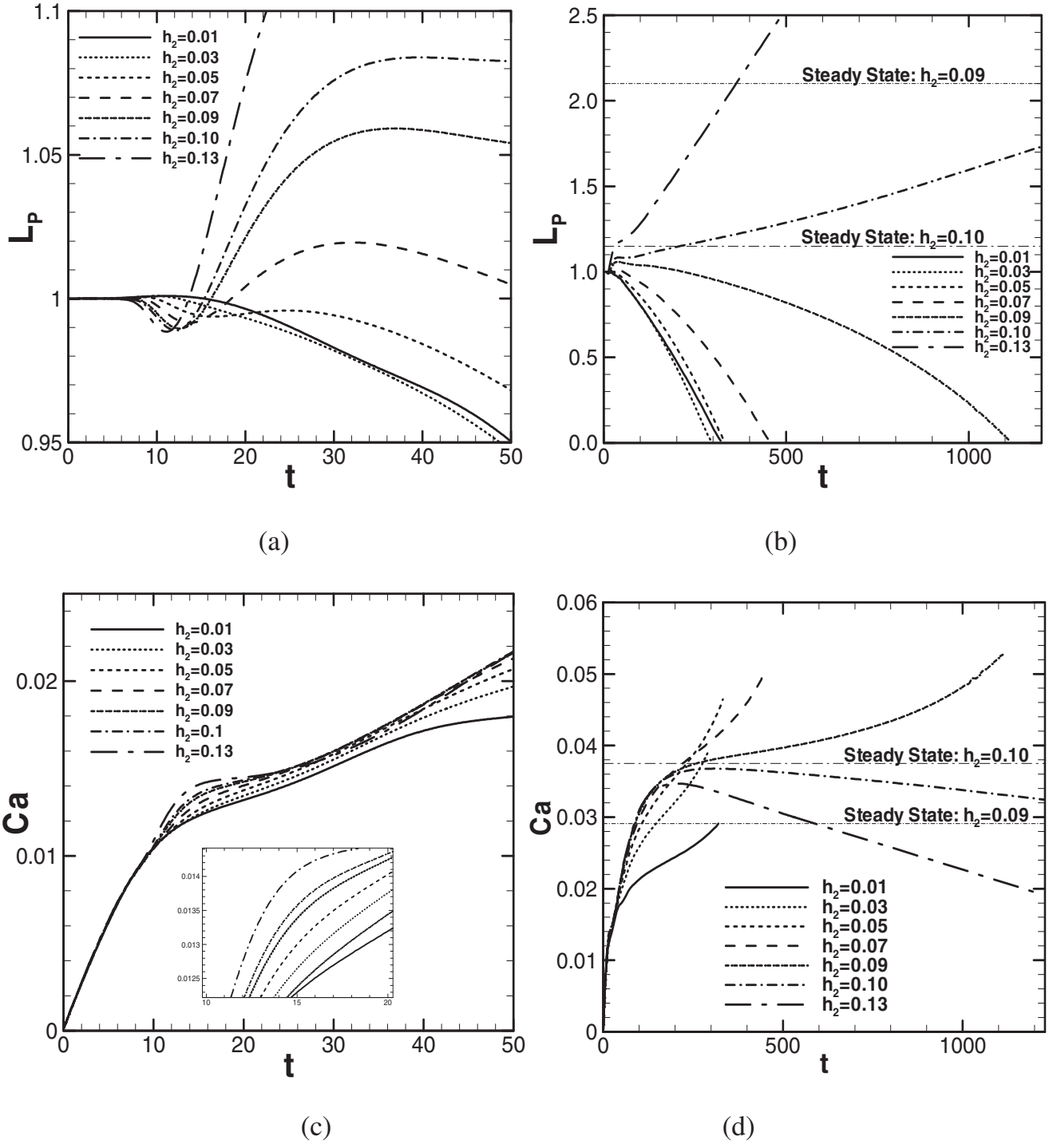

FIG. 2. Course of plug length and speed for different precursor film thicknesses. $\Delta P=1$, $L_{P0}=1$, and $\lambda=1000$. When $L_P\rightarrow 0$, $z_P\rightarrow 7.24$, 8.17, 10.5, 16.1, and 44.4 for $h_2=0.01$, 0.03, 0.05, 0.07, and 0.09.

course of L_P is plotted in Figs. 2(a) and 2(b), where (a) is a magnified plot for $0<t<50$ of (b). The course of Ca is plotted in (c) and (d) in the same manner. At $t=0$, a constant pressure drop across the plug, $\Delta P=1$, is prescribed and the plug begins to propagate. The dimensionless plug speed is $\mathrm{Ca}=\mu U/\sigma_M$, where U is defined as the average of u_z^* at both meniscus tips. Here we examine the plug propagation for seven different values of the precursor film thickness h_2. When the trailing film thickness is thicker than h_2, the plug loses mass and L_P decreases. On the other hand, when the trailing film thickness is thinner than h_2, the plug gains mass and L_P increases.

According to the steady plug propagation analysis, the trailing film thickness is mainly a function of the capillary number Ca.[33] The steady solutions for $h_2=0.09$ and 0.10 are plotted in Figs. 2(b) and 2(d), which are obtained by applying the procedure described in Ref. 33. At $t=0$, the plug is accelerated by the pressure difference across it, and Ca in-

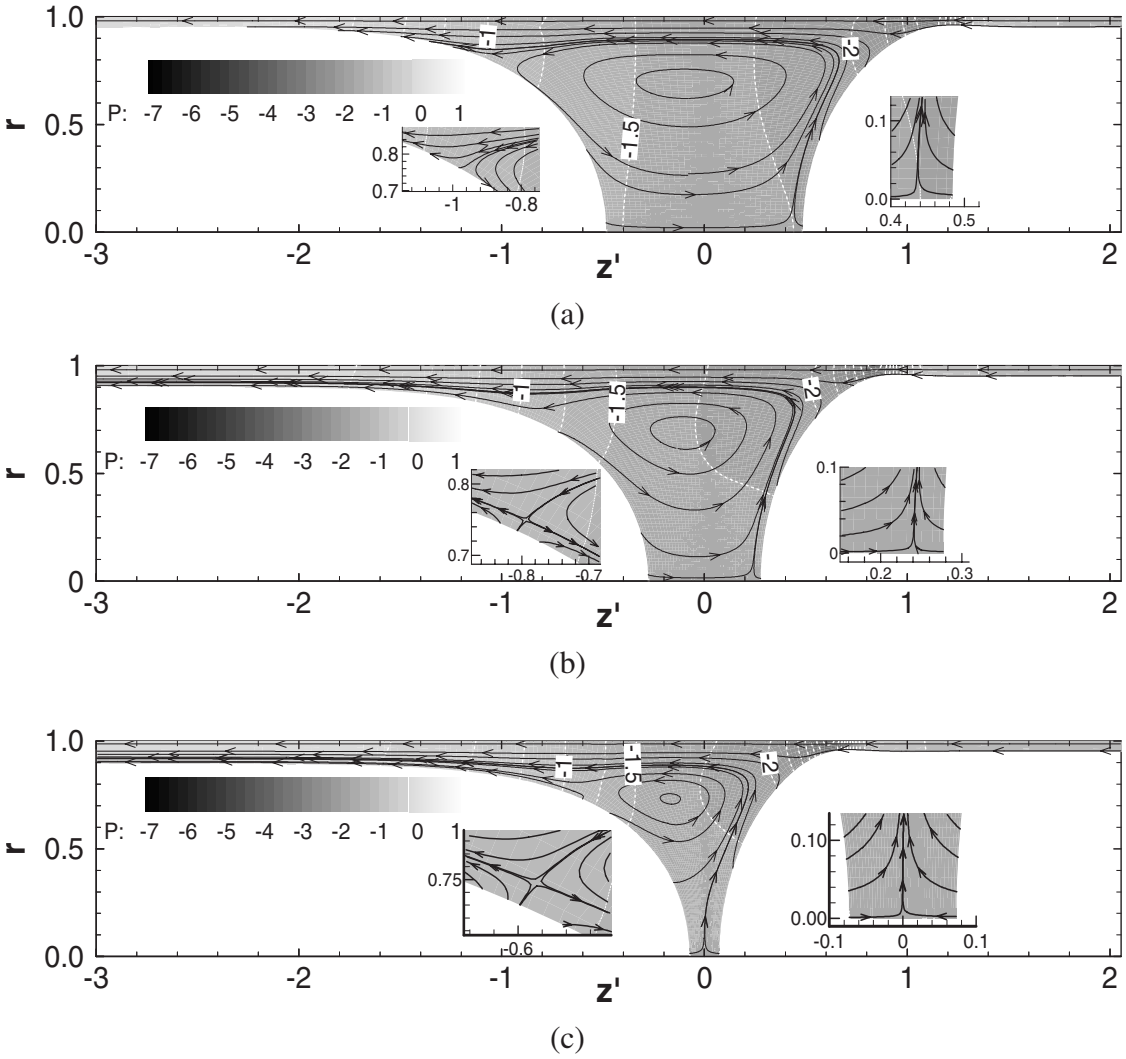

FIG. 3. Flow and pressure field for $h_2=0.05$. $\Delta P=1$, $L_{P0}=1$, $\lambda=1000$. (a) $t=50$; $L_P=0.97$; Ca=0.021, $z_P=0.70$. (b) $t=200$; $L_P=0.55$, Ca=0.036, $z_P=5.18$, and (c) $t=300$; $L_P=0.15$, Ca=0.043, and $z_P=9.06$.

creases. Figure 2(a) shows that, for $0<t<8$, L_P for all h_2 (except for $h_2=0.13$) remains almost unchanged; then L_P for $h_2\geqslant 0.05$ is locally minimum between $10<t<20$ and maximum in between $20<t<40$. For $h_2\leqslant 0.03$, L_P is maximum in between $10<t<15$. Up to $t\sim 100$, the initial disturbance in L_P decays. For $t>100$, L_P increases for $h_2\geqslant 0.10$ or decreases for $h_2\leqslant 0.09$ [Fig. 2(b)]. Figure 2(c) shows that, until $t\sim 10$, Ca for all h_2 increases similarly. For $10<t<20$, the slope of the increasing Ca becomes gentle in turn from smaller h_2, and then Ca increases with similar slope until $t\sim 40$. Figure 2(d) shows that, until $t\sim 50$, Ca increases almost similarly. For $t>50$, the slope of Ca for $h_2\leqslant 0.05$ becomes gentle compared to the slope for $h_2\geqslant 0.07$. Ca for $h_2\geqslant 0.07$ increases similarly until $t\sim 150$. For $h_2\geqslant 0.10$, Ca begins to decrease for $t>150$ because the total viscous resistance within the plug core increases due to the rising L_P, as Fig. 2(b) shows.

Compared with the steady solution for $h_2=0.10$, where $h_1=0.10$, $\Delta P=1.0$, $\lambda=1000$, $L_{P,S}=1.15$, and $\mathrm{Ca}_S=0.0375$ shown in Figs. 2(b) and 2(d), the unsteady solution of Ca for $h_2=0.10$ increases close to Ca_S but decreases without attaining to Ca_S after L_P becomes greater than $L_{P,S}$. For $h_2\leqslant 0.09$, after the initial disturbance, for $t>100$, L_P decreases since the trailing film thickness becomes thicker than h_2 as Ca increases. For these cases, L_P decreases toward zero resulting in plug rupture. In this computational model, however, the moment of plug rupture cannot be resolved. We stopped the computation when it meets the condition described in Sec. II F. For $h_2=0.01$, 0.03, 0.05, 0.07, and 0.09, this happened when $L_P=2.97\times 10^{-3}$, 4.04×10^{-3}, 4.23×10^{-3}, 4.85×10^{-3}, and 4.75×10^{-3}. The decreasing rate of L_P can be determined by the difference between the precursor and trailing film thicknesses multiplied by the plug speed, Ca. So, basically, the plug ruptures earlier for smaller h_2. However, since Ca at a fixed t decreases as h_2 decrease, the rate of mass loss for $h_2=0.01$ is smaller than that for $h_2=0.03$. Thus, the time to rupture for $h_2=0.01$ is longer than for $h_2=0.03$. Compared with the steady solution for $h_2=0.09$, where $h_1=0.09$, $\Delta P=1.0$, $\lambda=1000$, $L_{P,S}=2.1$, and $\mathrm{Ca}_S=0.0291$, the unsteady solution of Ca for $h_2=0.09$ increases and becomes larger than Ca_S; therefore, L_P decreases without reaching $L_{P,S}$.

Figure 3 shows snapshots of the streamlines and pressure fields at (a) $t=50$, (b) $t=200$, and (c) $t=300$ for $h_2=0.05$ of

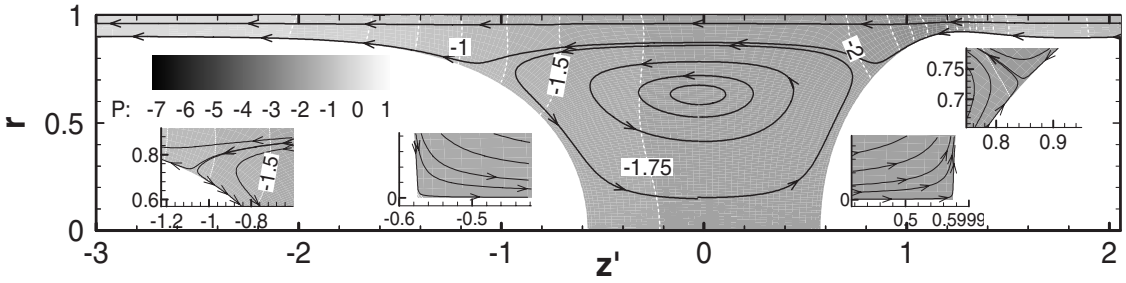

FIG. 4. Flow and pressure field for the steady propagation of plug. $h_1=h_2=0.10$, $\Delta P=1$, $\lambda=1000$, $L_{P,S}=1.15$, and $\mathrm{Ca}_S=0.0375$.

which L_P and Ca are shown in Fig. 2. The horizontal axis for each plot, $z'=z-z_P$, is a relative coordinate, where z_P is at the middle of both meniscus tips. The streamlines are drawn in the velocity field relative to the plug speed, Ca; the relative flow field is $(u_z-\mathrm{Ca},u_r)$, where Ca is the average of u_z at both meniscus tips. In the film far ahead or behind the plug, since the liquid is static, the relative velocity is $(-\mathrm{Ca},0)$. Thus, the streamlines in these static regions distribute corresponding to uniform flow. In the core, the streamline pattern shows a recirculation. Some streamlines that start from the meniscus interface are directed toward the trailing film, which indicates that the plug is losing mass.

At $t=50$, some of the streamlines end on the rear interface (see close-up plot). This indicates that this region of the rear interface is moving outward and the rear meniscus is elongating toward the tube axis. On the tube center axis, an inner stagnation point appears near the front interface tip (see close-up plot). A saddle point appears in the rear transition region at $t=200$ and 300 [see close-up plots in Figs. 3(b) and 3(c)]. When the plug length becomes very short, at $t=300$, $L_P=0.15$ [Fig. 3(c)], the inner stagnation point on the tube centerline is located at the middle of both tips.

In this study, since the pressure in the front air phase is set to zero as a reference pressure, the pressure in the precursor film far ahead of the plug is $-(1-h_2)^{-1}$. The pressure in the rear air phase is $P_1=1$, so the pressure in the trailing film is approximately $1-(1-h_1)^{-1}$. In the plug core, the pressure is lower due to the surface tension on the curved interface. The pressure is lowest at the front transition region between the front meniscus and the precursor film. From the core near the rear meniscus to the trailing film, the liquid pressure increases in the transition region. Because at $t=50$ both meniscus shapes are still deforming from the initial hemisphere shape, the pressure profile in both transition regions changes between $t=50$ and 200. Between $t=200$ and 300, the pressure fields in both transition regions are almost the same.

If the trailing film thickness matches exactly the precursor film thickness, L_P remains constant with time. Figure 4 shows the streamlines and pressure fields for the steady plug propagation of $h_2=0.10$. There are four stagnation points appearing on the interface in the half plug domain, which are at the meniscus tips and off the tips.[33]

Figure 5 shows the instantaneous streamline and pressure fields at $t=300$ for $h_2=0.13$. For this case, L_P increases as the plug propagates since the trailing film thickness is much thinner than h_2 [Fig. 2(b)]. Since L_P increases, some of the streamlines intercept on the interfaces, but the streamline pattern is different from the case shown in Fig. 3 in which L_P is decreasing. Figure 5 shows a saddle point that appears near the front meniscus interface and an inner stagnation point that appears on the centerline near the rear meniscus. The locations of the saddle and stagnation points are on the opposite side, as compared to those in Figs. 3(b) and 3(c).

Figure 6 shows an instantaneous profile of (a) the streamlines and pressure field and (b) the velocity and pressure field in the precursor film near the front meniscus for $h_2=0.03$ at $t=232$. The plug length is $L_P=0.3$. In the core, a recirculation is observed in the streamline pattern. Some streamlines that start at the meniscus interface are directed toward the trailing film, indicating that the plug is losing mass. The pressure is lowest where the front meniscus interface contacts to the precursor film. The details for this are shown in Fig. 6(b), where the velocity profiles (u_z,u_r) and the pressure field within $0.5<z'<0.82$ are plotted. The velocity is zero at $r=1.0$ due to the no-slip condition. For $z'<0.68$, the velocity vectors are directed toward the z'-positive direction since the pressure gradient for z',

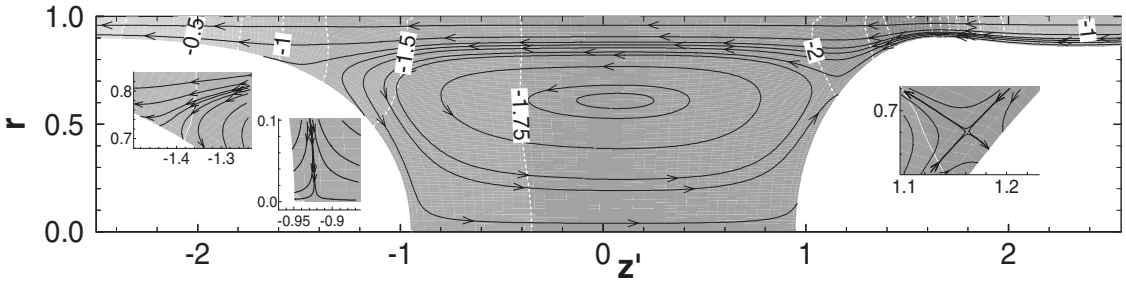

FIG. 5. Streamline and pressure field at $t=300$ for $h_2=0.13$. $\Delta P=1$, $L_{P0}=1$, $L_P=1.90$, $\mathrm{Ca}=0.034$, and $z_P=8.87$.

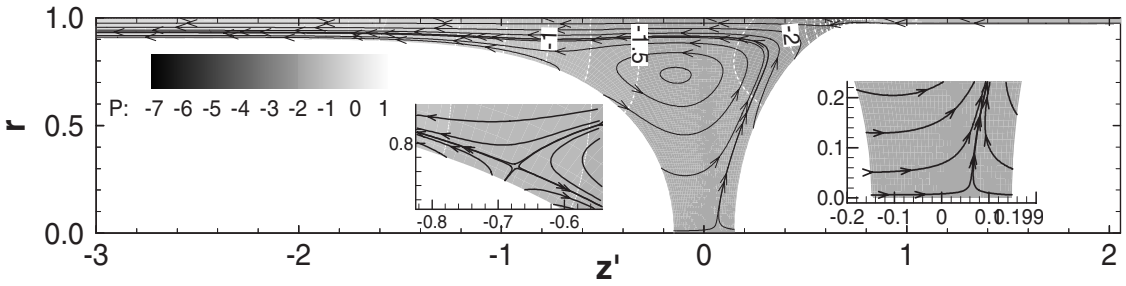

(a)

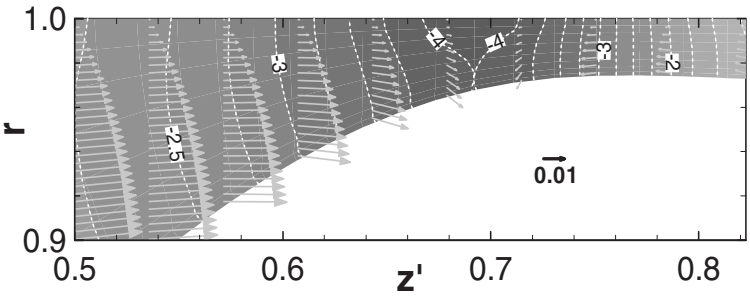

(b)

FIG. 6. Flow and pressure field for $h_2=0.03$ when $L_P=0.3$. $t=232$, $h_2=0.03$, $\Delta P=1$, $L_{P0}=1$, $\lambda=1000$, and Ca=0.034. (a) The relative flow streamline and pressure field. (b) The velocity profiles and pressure field in the precursor film near the front meniscus.

$\partial p/\partial z'$, is negative. The pressure is minimum at $z'=0.69$, and $\partial p/\partial z'$ for $z>0.71$ is positive. This induces the flow to be directed toward the z'-negative direction. Since the fluid in this region is drained by this reverse flow, the film is a minimum thickness at $z'=0.76$ where the reverse flow velocity is maximum.

For $h_2=0.01$, as shown in Fig. 7(a), the streamline pattern and the pressure profiles are similar to those for the h_2

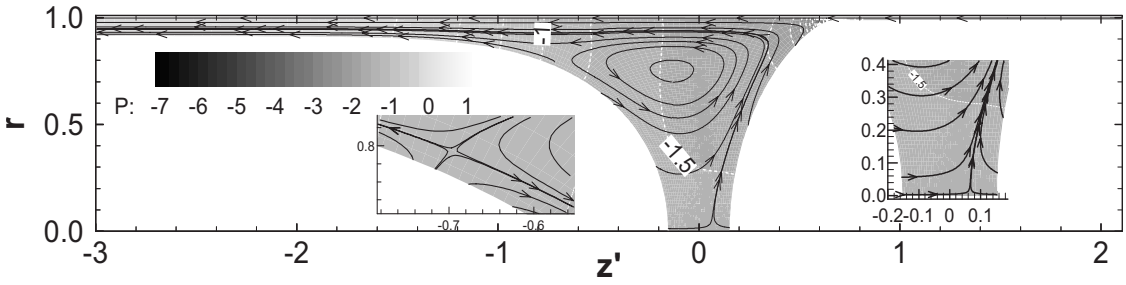

(a)

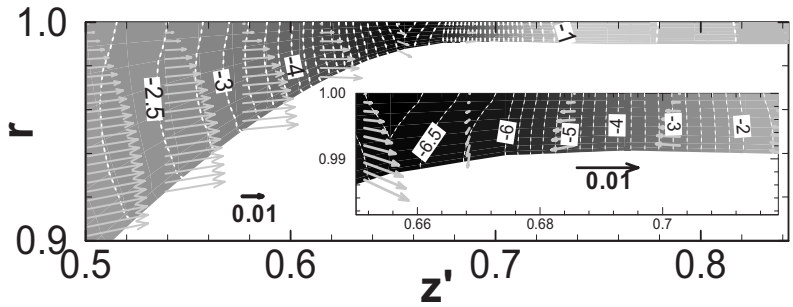

(b)

FIG. 7. Flow and pressure field for $h_2=0.01$ when $L_P=0.3$. $t=245$, $h_2=0.01$, $\Delta P=1$, $L_{P0}=1$, $\lambda=1000$, and Ca=0.026. (a) The relative flow streamlines and pressure field. (b) The velocity profiles and pressure field in the precursor film near the front meniscus.

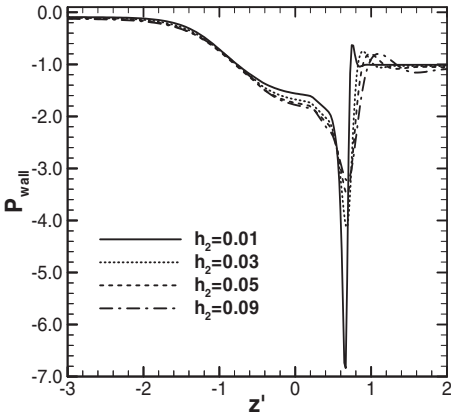

FIG. 8. Wall pressure distributions when $L_P=0.3$. $\Delta P=1$, $L_{P0}=1$, and $\lambda=1000$. For $h_2=0.01$, $t=245$, Ca=0.026, and $z_P=5.05$; for $h_2=0.03$, $t=232$, Ca=0.034, and $z_P=5.82$; for $h_2=0.05$, $t=263$, Ca=0.040, and $z_P=7.54$; for $h_2=0.09$, $t=959$, Ca=0.047, and $z_P=36.5$.

$=0.03$ case. In this case, the plug length becomes $L_P=0.3$ at $t=245$. The pressure is smallest at $z'=0.66$. Figure 7(b) shows that the minimum pressure value is even smaller than that for $h_2=0.03$. The flow pattern is similar to that for $h_2=0.03$, but the velocity gradient in r is much steeper because of the thinner precursor film thickness.

B. Wall pressure and shear stress

Figure 8 shows the pressure distributions along the wall for $h_2=0.01$, 0.03, 0.05, and 0.09 at $t=245$, 232, 263, and 959, respectively. At these times, the plug length for each becomes $L_P=0.3$. The plug speeds at these times are Ca $=0.026$, 0.034, 0.040, and 0.047. P_{wall} is minimum in the front transition region around $z'=0.63-0.65$. The absolute value of this negative peak in P_{wall} increases as h_2 decreases. The pressure gradient around the peak becomes steeper as well.

Figure 9 shows the dimensionless wall shear stress distributions for the cases shown in Fig. 8. The wall shear stress, $\tau_w=\partial u_z/\partial r$, in both ends is zero because both films are

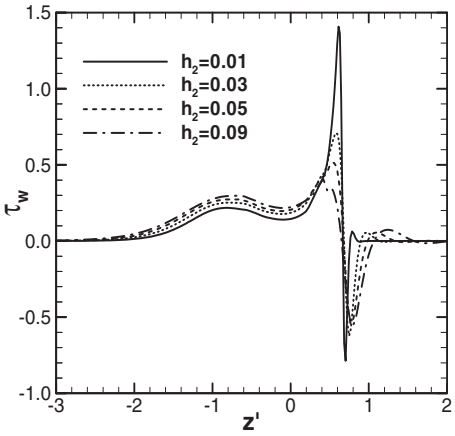

FIG. 9. Wall shear stress distributions when $L_P=0.3$. $\Delta P=1$, $L_{P0}=1$, and $\lambda=1000$. For $h_2=0.01$, $t=245$, Ca=0.026, and $z_P=5.05$; for $h_2=0.03$, $t=232$, Ca=0.034, and $z_P=5.82$; for $h_2=0.05$, $t=263$, Ca=0.040, and $z_P=7.54$; for $h_2=0.09$, $t=959$, Ca=0.047, and $z_P=36.5$.

static at the far ends. In the front meniscus region, $z'=0.5-0.7$, τ_w has peaks for both positive and negative directions because the direction of u_z changes in this region, as shown in Figs. 6 and 7. The sign of τ_w changes at the point where the pressure is lowest. The absolute values of the positive and negative peaks increase as h_2 decreases. The positive peaks appear at $z'=0.6$ for $h_2=0.03$ and 0.01. At this location, Figs. 6(b) and 7(b) show that the distance between the meniscus surface and the tube wall is narrower for $h_2=0.01$ than for $h_2=0.03$. Since the gap between the moving front meniscus surface and the tube wall is narrower for smaller h_2, the positive peak of τ_w increases. The plug speeds decrease as h_2 decreases, but the narrowing gap increases the shear rate at these points. The drag force is the integration of τ_w; thus, the flow resistance increases in this region significantly as h_2 decreases. In the rear meniscus transition region and the plug core, $z'=-2.0-0.2$, the difference in τ_w for h_2 is insignificant. As h_2 increases, Ca increases but τ_w increases weakly because the trailing film thickness increases with Ca and the wall shear rate does not increase as much as Ca.

C. Initial plug length

Figure 10 shows the effect of the initial plug length L_{P0} on plug length and speed as a function of time for $L_{P0}=0.5$, 1, 2, and 15. The remaining parameters are fixed as $\Delta P=1$, $\lambda=1000$, and $h_2=0.05$. The steady solution of $L_{P,S}=11$, $\lambda=1000$, $h_2=0.05$, $\Delta P=1$, and $\text{Ca}_s=0.0093$ is plotted for comparison. As L_{P0} increases, since the total mass of the plug and the viscous resistance in the core region also increase, the initial acceleration decreases. The plug speed at the time of rupture is almost independent of L_{P0}. The time to rupture is not a simple linear function of L_{P0}. Comparing $L_{P0}=1$ and 2, the rupture time for $L_{P0}=2$ is more than twice that for $L_{P0}=1$. For $L_{P0}=0.5$, 1, and 2, the times that the decreasing L_P becomes 0.25 (corresponding $L_P/L_{P0}=0.5$, 0.25, and 0.125) are $t=97.8$, 277, and 792, respectively. The corresponding Ca are 0.0377, 0.0406, and 0.0407, respectively. Since the plugs with $L_{P0}=1$ and 2 propagate with almost the same speed, the influence of the initial condition can be considered to be diminished by this time. If L_{P0} is sufficiently long, there will not be a sufficiently large value of Ca at which the trailing film becomes thicker than the precursor film. A critical value of L_{P0} can exist at which the plug may not rupture under fixed ΔP and h_2. If Ca is maintained below the steady solution value, which is $\text{Ca}_s=0.008$ under the condition in Fig. 10, the trailing film thickness is always less than $h_2=0.05$. The steady solution is achieved when $L_{P,S}=11$. Therefore, if $L_P>11$, L_P increases as the plug propagates. For $L_{P0}=15$, Ca increases, then decreases for $t>900$ without attaining 0.008 because of the large viscous resistance in the core.

D. Pressure drop

Figure 11 shows the plug length and speed versus time for three different values of the pressure drop across the plug, $\Delta P=1$, 0.5, and 0.1. The remaining parameters are fixed as $L_{P0}=1$, $\lambda=1000$, and $h_2=0.05$. The steady solution of $L_{P,S}=1$, $\lambda=1000$, $h_2=0.05$, $\Delta P=0.36$, and $\text{Ca}_S=0.0093$ is

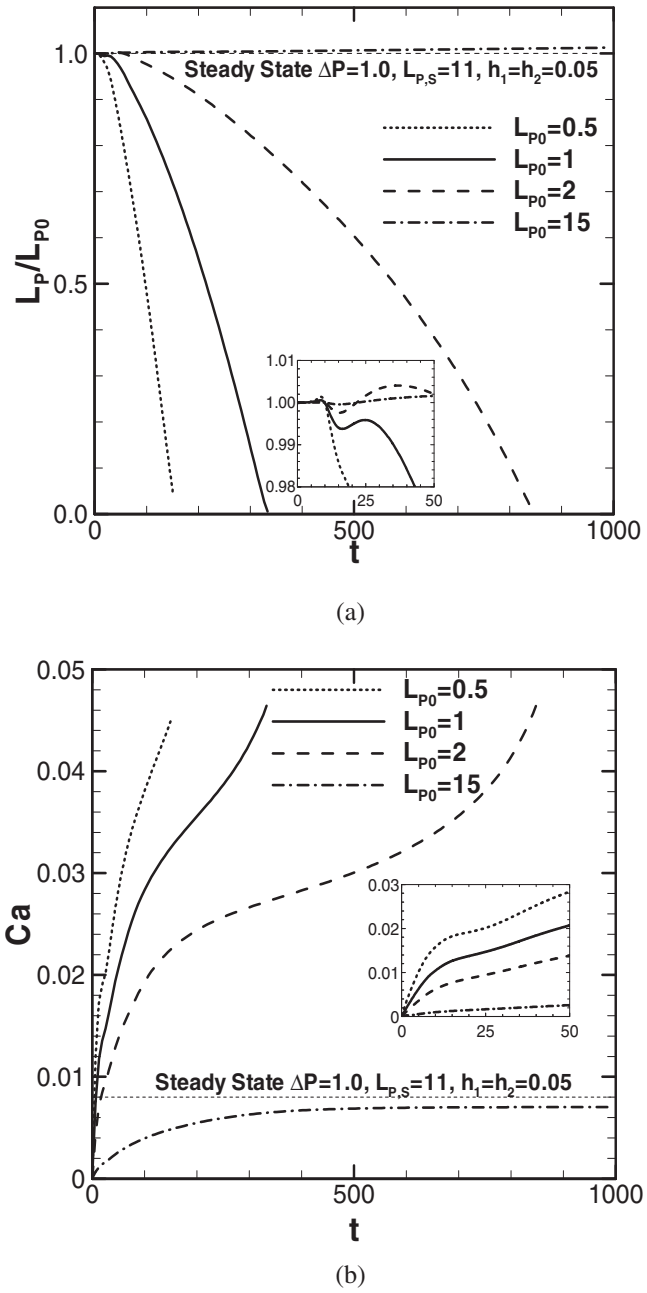

FIG. 10. Course of plug length (L_P/L_{P0}) and speed for three different initial plug lengths. $\Delta P=1$, $\lambda=1000$, and $h_2=0.05$. When $L_P\to 0$, $z_P\to 4.78$, 10.5, and 24.2 for $L_{P0}=0.5$, 1, and 2.

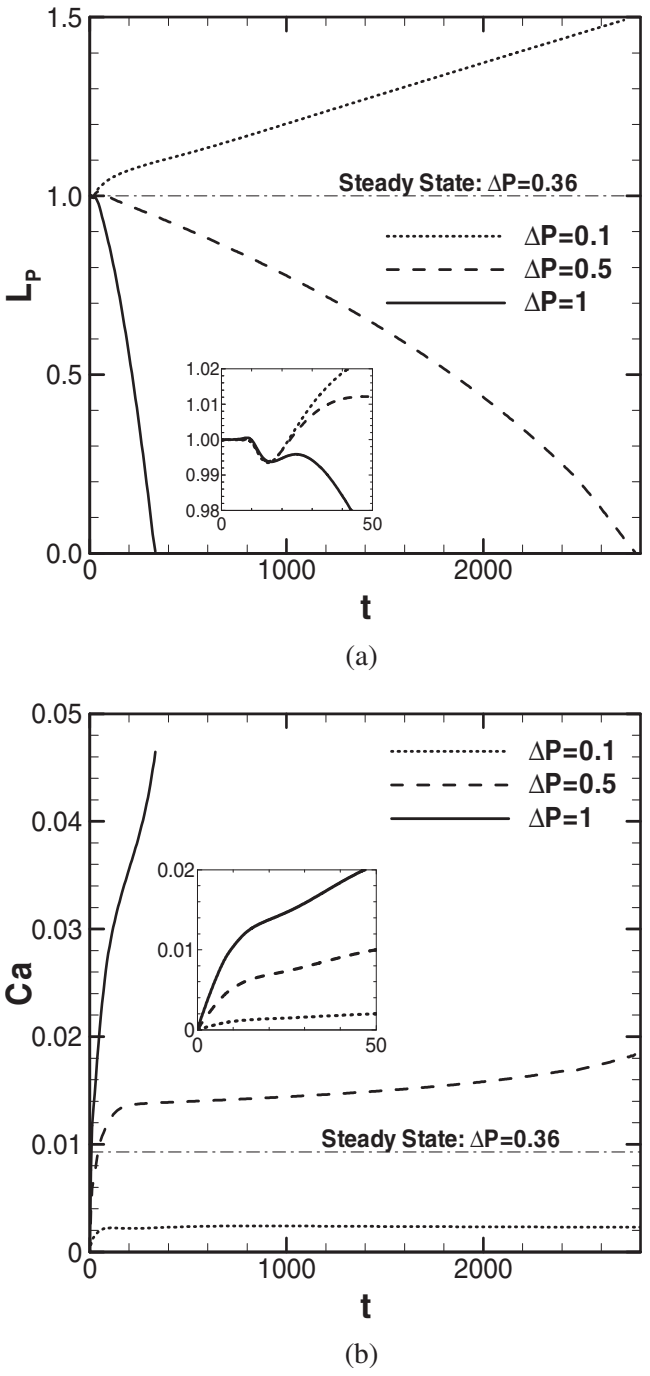

FIG. 11. Course of plug length and its speed for different pressure drop across the plug. $L_{P0}=1$, $\lambda=1000$, and $h_2=0.05$. When $L_P\to 0$, $z_P\to 10.5$ and 41.5 for $\Delta P=1$ and 0.5.

plotted for comparison. For all cases, L_P decreases then increases initially, then it decreases (or increases) monotonically [see close-up in Fig. 11(a)]. For $\Delta P=1$, the plug speed, Ca, increases with the steepest slope among these three cases. So the plug length L_P decreases toward zero with the shortest time among them. For $\Delta P=0.5$, L_P goes to zero, but it takes a longer time than for $\Delta P=1$. For $\Delta P=0.5$, the Ca curve is quite different from that for $\Delta P=1$; Ca increases initially, and then remains almost unchanged, indicating that ΔP balances with the viscous dissipation across the plug. For $\Delta P=0.5$, L_P continues to decrease since the trailing film is thicker than the precursor film of $h_2=0.05$ for this level of Ca$\sim$0.015. Since the plug shortens, the viscous resistance in the core decreases gradually and Ca gently increases as the plug propagates. For the steady solution, $\mathrm{Ca}_S=0.0093$, the trailing film thickness equals h_2. Thus, for $\mathrm{Ca}<\mathrm{Ca}_S$, the trailing film thickness is smaller than h_2 and the plug persists propagating without rupture. For $\Delta P=0.1$, L_P increases and Ca plateaus at an even smaller value than for $\Delta P=0.5$. For this plateau level of Ca which is less than Ca_S, the trailing film thickness is thinner than the precursor film thickness, $h_2=0.05$. Since this plug elongates, the viscous resistance in the core increases and Ca gently decreases as it propagates. For a fixed L_{P0} and h_2, a critical value of ΔP can exist, above which the plug will rupture.

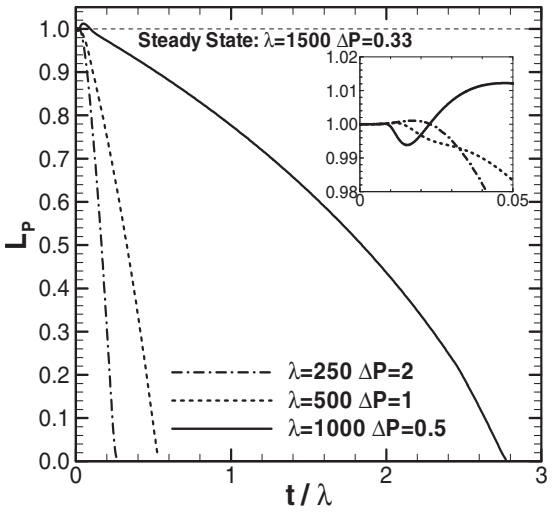

(a)

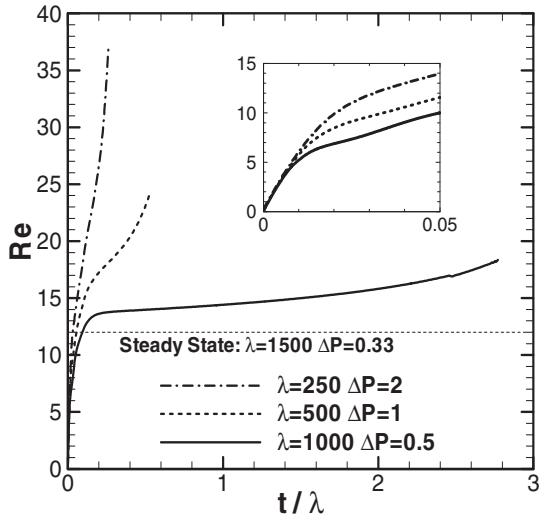

(b)

FIG. 12. Course of plug length and its speed for surface tensions. $L_{P0}=1$, $\Delta P\lambda=500$, and $h_2=0.05$. When $L_P\rightarrow 0$, $z_P\rightarrow 5.45$, 8.02, and 41.5 for $\lambda=250$, 500, and 1000.

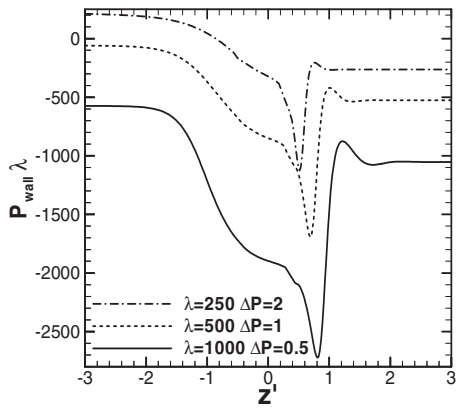

(a)

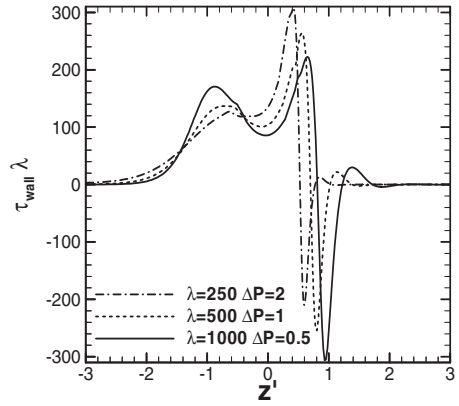

(b)

FIG. 13. Wall pressure and shear stress distributions for different surface tensions. $L_{P0}=1$, $\Delta P\lambda=500$, and $h_2=0.05$. $L_P=0.3$ for all, Re=26, 21, and 17 at $t/\lambda=0.20$, 0.42, and 2.3 for $\lambda=250$, 500, and 1000.

E. Effect of surface tension

The effect of surface tension on plug propagation is examined for a fixed pressure drop and precursor film thickness. Since the dimensionless parameters, λ and ΔP, depend on the surface tension, these parameters are chosen at a fixed $\Delta P\lambda=\Delta P^*(\rho R^2/\mu^2)$ so that ΔP^*, ρ, R, and μ are fixed. Figure 12 shows the plug length and speed versus time for three different surface tension cases at a fixed pressure drop, $\Delta P\lambda=500$, $h_2=0.05$, and $L_{P0}=1$. As λ increases, the surface tension on the interface increases. The time is rescaled as $t/\lambda=t^*[\mu/(\rho R^2)]$; the dimensionless plug speed is redefined as $\mathrm{Re}=\mathrm{Ca}\lambda=\rho RU/\mu$, which is the Reynolds number. The steady solution of $L_{P,S}=1$, $\lambda=1500$, $h_2=0.05$, $\Delta P=0.33$, and $\mathrm{Re}_S=12$ is plotted for comparison. For all cases, after the initial transition in L_P [see close-up in Fig. 12(a)], L_P decreases with time and eventually the plug ruptures. The time to plug rupture is longer for larger λ, which indicates that a larger surface tension delays plug rupture. Since the plug speed, Re, at a fixed time is larger for smaller λ [Fig. 12(b)], L_P decreases more rapidly for the smaller surface tension case. Also, since the capillary number, $\mathrm{Ca}=\mathrm{Re}/\lambda$, is larger for smaller λ, the trailing film thickness is thicker for the smaller surface tension case. The total distances that the plug propagates are $z_P=5.45$, 8.02, and 41.5 for $\lambda=250$, 500, and 1000, respectively. The plug propagation length increases with λ because the smaller rate of mass loss results in a longer time for plug propagation. If the surface tension is larger than the steady solution as $\lambda>1500$ and $\Delta P<0.33$, the trailing film thickness is smaller than h_2 and the plug will persist in propagation without rupture, which is similar to the $\Delta P=0.1$ case shown in Fig. 11.

Figure 13 shows the wall pressure and shear stress distributions when $L_P=0.3$ for three different surface tension cases. The plug speeds are Re=26, 21, and 17 at $t/\lambda=0.20$, 0.42, and 2.3 for $\lambda=250$, 500, and 1000, respectively. The dimensionless pressure and shear stress are rescaled as $P_{\mathrm{wall}}\lambda=P^*_{\mathrm{wall}}(\rho R^2/\mu^2)$ and $\tau_{\mathrm{wall}}\lambda=\tau^*_{\mathrm{wall}}(\rho R^2/\mu^2)$. As the surface tension increases, the pressures in both the precursor and trailing films decrease because the net force of the circumferential component of the surface tension reduces the liquid pressure. As the surface tension increases, the negative

peak in pressure that appears in the front transition region decreases (more negative), and the steep pressure gradient around the peak becomes even greater. In the rear transition region, the pressure gradient becomes steeper with λ. For the wall shear stress, since the plug speed decreases as the surface tension increases, the positive peak in wall shear stress in the front region decreases. The capillary numbers for these cases are Ca=0.11, 0.041, and 0.017 for λ=250, 500, and 1000. Since the minimum film thickness in the front transition region decreases as Ca decreases,[33,44,45] the negative peak in wall shear stress decreases (more negative) as the surface tension increases. In the rear transition region, the positive peak and the wall shear stress gradient increase with surface tension.

IV. DISCUSSION

When a liquid plug propagates through lung airways, airway epithelial cells are damaged by excessive mechanical stresses induced by the motion of fluid and surface tension.[5–7] In this study, we have shown that the strength of the wall pressure and shear stress in the front transition region of the plug increases as the precursor film thins. The magnitude of these stresses is much larger than those in the rear transition region. Assuming an airway of $R \sim 0.2$ cm and $\sigma_M \sim 50$ dyn/cm in a surfactant-reduced lung, the dimensional shear stresses for $h_2=0.01$ and Ca=0.026 shown in Fig. 9 are about 50 dyn/cm^2 at $z'=-0.8$ in the rear transition region and 350 dyn/cm^2 at $z'=0.6$ in the front transition region where τ_w attains a positive peak. The pressure gradient in the front transition region is extremely large; the maximum $\partial P_{\text{wall}}/\partial z$ is 104 with a dimensional value of 13 dyn cm$^{-2}/\mu$m. These values are large enough to induce lung epithelial cell damage.[5,6]

As the surface tension increases, since the total resistance across the plug increases, the plug propagation speed decreases for a constant pressure drop across the plug, but the plug propagates a longer distance (see Fig. 12) since the trailing film is thinner. The wall pressure within the plug varies significantly and the variation increases as the surface tension increases (see Fig. 13). The wall pressure peaks in the front transition region. The magnitude of the peak wall pressure increases and the pressure gradient around the peak becomes even steeper as the surface tension increases. In the rear transition region, the pressure gradient also becomes steeper as the surface tension increases. When lung-surfactant availability is reduced, liquid plugs form and propagate more frequently.[4] Therefore, airway epithelial cell damage may occur with higher probability for a larger region of an airway in surfactant-reduced lungs due to diseases such as respiratory distress syndrome (RDS). Lung airway length is approximately four to eight times the airway radius.[46] For most of the cases investigated in this study, the distance that plugs propagate until rupture is longer than the airway length. Hence, the plug will split at bifurcations into two shorter plugs and continue propagating into the two daughter tubes.[47,48]

The plug gains fluid from the leading front film and deposits fluid into the trailing film. If the trailing film is thicker than the precursor film, the plug volume decreases as it propagates and the plug will finally rupture. Although the trailing film thickness varies as functions of Ca, Re, and L_P, it is primarily dependent on Ca.[33] In this study, since we investigate unsteady plug propagation driven by a constant pressure drop across the plug, Ca varies with time, and it depends on the inertia and the resistance in the plug. The resistance across the plug can roughly be divided into three regional contributions; the front transition region, the core region, and the rear transition region. The resistance in the front transition region varies depending on the precursor film thickness. As Fig. 8 shows, the positive peak in wall shear stress within the front transition region increases as h_2 decreases, indicating an increase in the resistance. The resistance in the core region depends on the plug length L_P. Assuming Poiseuille flow in the core, the resistance is a linear function of L_P. In the rear transition region, although the wall shear stress increases as Ca increases, the resistance decreases because the trailing film thickness increases with Ca.

When a plug propagates in a steady state under a given ΔP, h_2, and λ, the plug length $L_{P,S}$ must be a definite length so that there is enough resistance in the core region to maintain the plug speed to be Ca_S, which causes the trailing film thickness to equal h_2. When ΔP increases (decreases) slightly from a steady state, Ca increases (decreases) and consequently h_1 increases (decreases), and hence L_P decreases (increases) as the plug propagates. Since the resistance in the core decreases (increases) as L_P decreases (increases), Ca increases (decreases) further. This may be similar when h_2 increases (decreases) slightly from a steady state. Since h_1 is less (greater) than h_2, L_P increases (decreases). Ca decreases (increases) as L_P increases (decreases), which causes h_1 to decrease (increase). So h_1 becomes even smaller (larger) than h_2. To clarify a stability criterion, further analysis is required.[49]

ACKNOWLEDGMENTS

The authors would like to thank Dr. Zierenberg and Dr. Bian for reading the manuscript. This work is supported by NIH Grant Nos. HL84370, HL64373, and HL85156, and NASA Grant No. NBEI-NNC04AA21A.

[1] J. M. B. Hughes, D. Y. Rosenzweig, and P. B. Kivitz, "Site of airway closure in excised dog lungs: Histologic demonstration," J. Appl. Physiol. **29**, 340 (1970).
[2] P. T. Macklem, D. F. Proctor, and J. C. Hogg, "The stability of peripheral airways," Respir. Physiol. **8**, 191 (1970).
[3] R. D. Kamm and R. C. Schroter, "Is airway closure caused by a thin liquid instability?" Respir. Physiol. **75**, 141 (1989).
[4] D. Halpern and J. B. Grotberg, "Fluid-elastic instabilities of liquid-lined flexible tubes," J. Fluid Mech. **244**, 615 (1992).
[5] A. M. Bilek, K. C. Dee, and D. P. Gaver, "Mechanisms of surface-tension-induced epithelial cell damage in a model of pulmonary airway reopening," J. Appl. Physiol. **94**, 770 (2003).
[6] S. S. Kay, A. M. Bilek, K. C. Dee, and D. P. Gaver, "Pressure gradient, not exposure duration, determines the extent of epithelial cell damage in a model of pulmonary airway reopening," J. Appl. Physiol. **97**, 269 (2004).
[7] D. Huh, H. Fujioka, Y. C. Tung, N. Futai, R. Paine III, J. B. Grotberg, and S. Takayama, "Acoustically detectable cellular-level lung injury induced by fluid mechanical stresses in microfluidic airway systems," Proc. Natl. Acad. Sci. U.S.A. **104**, 18886 (2007).

[8]B. Robertson, "Surfactant replacement therapy for severe neonatal respiratory distress syndrome: An international randomized clinical trial," Pediatrics **82**, 683 (1988).
[9]W. Long, T. Thompson, H. Sundell, R. Schumacher, F. Volberg, and R. Guthrie, "Effects of two rescue doses of a synthetic surfactant on mortality rate and survival without bronchopulmonary dysplasia in 700- to 1350-gram infants with respiratory distress syndrome. The American Exosurf Neonatal Study Group I," J. Pediatr. (St. Louis) **118**, 595 (1991).
[10]E. M. Zola, J. H. Gunkel, R. K. Chan, M. O. Lim, I. Knox, B. H. Feldman, S. E. Denson, B. S. Stonestreet, B. R. Mitchell, M. M. Wyza, K. J. Bennett, and A. J. Gold, "Comparison of 3 dosing procedures for administration of bovine surfactant to neonates with respiratory-distress syndrome," J. Pediatr. (St. Louis) **122**, 453 (1993).
[11]H. Yapicioglu, D. Yildizdas, I. Bayram, Y. Sertdemir, and H. L. Yilmaz, "The use of surfactant in children with acute respiratory distress syndrome: Efficacy in terms of oxygenation, ventilation and mortality," Pulm. Pharmacol. Ther. **16**, 327 (2003).
[12]M. D. Salvia-Roiges, X. Carbonell-Estrany, J. Figueras-Aloy, and J. M. Rodriguez-Miguelez, "Efficacy of three treatment schedules in severe meconium aspiration syndrome," Acta Paediatr. **93**, 60 (2004).
[13]R. B. Hirschl, R. Tooley, A. C. Parent, K. Johnson, and R. H. Bartlett, "Improvement of gas exchange, pulmonary function, and lung injury with partial liquid ventilation. A study model in a setting of severe respiratory failure," Chest **108**, 500 (1995).
[14]T. H. Shaffer and M. R. Wolfson, "Liquid ventilation: An alternative ventilation strategy for management of neonatal respiratory distress," Eur. J. Pediatr. **155**, S30 (1996).
[15]H. P. Baden, J. D. Mellema, S. L. Bratton, P. P. O'Rourke, and J. C. Jackson, "High-frequency oscillatory ventilation with partial liquid ventilation in a model of acute respiratory failure," Crit. Care Med. **25**, 299 (1997).
[16]C. L. Leach, J. S. Greenspan, S. D. Rubenstein, T. H. Shaffer, M. R. Wolfson, J. C. Jackson, R. DeLemos, and B. P. Fuhrman, "Partial liquid ventilation with perflubron in premature infants with severe respiratory distress syndrome. The LiquiVent Study Group," N. Engl. J. Med. **335**, 761 (1996).
[17]K. Mikawa, K. Nishina, Y. Takao, and H. Obara, "Efficacy of partial liquid ventilation in improving acute lung injury induced by intratracheal acidified infant formula: Determination of optimal dose and positive end-expiratory pressure level," Crit. Care Med. **32**, 209 (2004).
[18]C. W. Choi, J. H. Hwang, Y. S. Chang, and W. S. Park, "Combined effect of low-dose nitric oxide gas inhalation with partial liquid ventilation on hemodynamics, pulmonary function, and gas exchange in acute lung injury of newborn piglets," J. Korean Med. Sci. **18**, 813 (2003).
[19]P. N. Cox, H. Frndova, O. Karlsson, S. Holowka, and C. A. Bryan, "Fluorocarbons facilitate lung recruitment," Intensive Care Med. **29**, 2297 (2003).
[20]D. J. Weiss, L. Bonneau, and D. Liggitt, "Use of perfluorochemical liquid allows earlier detection of gene expression and use of less vector in normal lung and enhances gene expression in acutely injured lung," Molecular Therapy **3**, 734 (2001).
[21]K. Nakazawa, K. Yokoyama, Y. Matsuzawa, K. Makita, and K. Amaha, "Pulmonary administration of prostacyclin (PGI(2)) during partial liquid ventilation in an oleic acid-induced lung injury: inhalation of aerosol or intratracheal instillation?" Intensive Care Med. **27**, 243 (2001).
[22]E. W. Dickson, S. O. Heard, T. E. Tarara, J. G. Weers, A. B. Brueggemann, and G. V. Doern, "Liquid ventilation with perflubron in the treatment of rats with pneumococcal pneumonia," Crit. Care Med. **30**, 393 (2002).
[23]J. Yu and Y. W. Chien, "Pulmonary drug delivery: Physiologic and mechanistic aspects," Crit. Rev. Ther. Drug Carrier Syst. **14**, 395 (1997).
[24]E. Raczka, J. F. Kukowska-Latallo, M. Rymaszewski, C. Chen, and J. R. Baker, "The effect of synthetic surfactant Exosurf on gene transfer in mouse lung in vivo," Gene Ther. **5**, 1333 (1998).
[25]A. H. Jobe, T. Ueda, J. A. Whitsett, B. C. Trapnell, and M. Ikegami, "Surfactant enhances adenovirus-mediated gene expression in rabbit lungs," Gene Ther. **3**, 775 (1996).
[26]O. E. Jensen, D. Halpern, and J. B. Grotberg, "Transport of a passive solute by surfactant-driven flows," Chem. Eng. Sci. **49**, 1107 (1994).
[27]Y. L. Zhang, O. K. Matar, and R. V. Craster, "A theoretical study of chemical delivery within the lung using exogenous surfactant," Med. Eng. Phys. **25**, 115 (2003).
[28]S. Iqbal, S. Ritson, I. Prince, J. Denyer, and M. L. Everard, "Drug delivery and adherence in young children," Pediatr. Pulmonol. **37**, 311 (2004).
[29]P. B. Myrdal, K. L. Karlage, S. W. Stein, B. A. Brown, and A. Haynes, "Optimized dose delivery of the peptide cyclosporine using hydrofluoroalkane-based metered dose inhalers," J. Pharm. Sci. **93**, 1054 (2004).
[30]K. J. Cassidy, J. L. Bull, M. R. Glucksberg, C. A. Dawson, S. T. Haworth, R. B. Hirschl, N. Gavriely, and J. B. Grotberg, "A rat lung model of instilled liquid transport in the pulmonary airways," J. Appl. Physiol. **90**, 1955 (2001).
[31]P. D. Howell, S. L. Waters, and J. B. Grotberg, "The propagation of a liquid bolus along a liquid-lined flexible tube," J. Fluid Mech. **406**, 309 (2000).
[32]S. L. Waters and J. B. Grotberg, "The propagation of a surfactant laden liquid plug in a capillary tube," Phys. Fluids **14**, 471 (2002).
[33]H. Fujioka and J. B. Grotberg, "Steady propagation of a liquid plug in a two-dimensional channel," J. Biomech. Eng. **126**, 567 (2004).
[34]H. Fujioka and J. B. Grotberg, "The steady propagation of a surfactant-laden liquid plug in a two dimensional channel," Phys. Fluids **17**, 082102 (2005).
[35]J. F. Thompson, B. K. Soni, and N. P. Weatherill, *Handbook of Grid Generation* (CRC, Boca Raton, 1999).
[36]P. Wesseling, A. Segal, C. G. M. Kassels, and H. Bijl, "Computing flows on general two-dimensional nonsmooth staggered grids," J. Eng. Math. **34**, 21 (1998).
[37]S. C. Xue, N. Phanthien, and R. I. Tanner, "Numerical study of secondary flows of viscoelastic fluid in straight pipes by an implicit finite-volume method," J. Non-Newtonian Fluid Mech. **59**, 191 (1995).
[38]S. Muzaferija and M. Peric, "Computation of free-surface flows using the finite-volume method and moving grids," Numer. Heat Transfer, Part B **32**, 369 (1997).
[39]W. H. Press, S. A. Teukolsky, W. T. Vellerling, and B. P. Flannery, *Numerical Recipes in C*, 2nd ed. (Cambridge University Press, Cambridge, 1992).
[40]J. W. Demmel, S. C. Eisenstat, J. R. Gilbert, X. Y. S. Li, and J. W. H. Liu, "A supernodal approach to sparse partial pivoting," SIAM J. Matrix Anal. Appl. **20**, 720 (1999).
[41]K. J. Cassidy, N. Gavriely, and J. B. Grotberg, "Liquid plug flow in straight and bifurcating tubes," J. Biomech. Eng. **123**, 580 (2001).
[42]D. Yager, T. Cloutier, H. Feldman, J. Bastacky, J. M. Drazen, and R. D. Kamm, "Airway surface liquid thickness as a function of lung volume in small airways of the guinea pig," J. Appl. Physiol. **77**, 2333 (1994).
[43]M. A. Sackner and C. S. Kim, "Phasic flow mechanisms of mucus clearance," Eur. J. Respir. Dis. Suppl. **153**, 159 (1987).
[44]F. P. Bretherton, "The motion of long bubbles in tubes," J. Fluid Mech. **10**, 166 (1961).
[45]M. D. Giavedoni and F. A. Saita, "The rear meniscus of a long bubble steadily displacing a Newtonian liquid in a capillary tube," Phys. Fluids **11**, 786 (1999).
[46]E. R. Weibel and D. M. Gomez, "Architecture of the human lung," Science **137**, 577 (1962).
[47]Y. Zheng, J. C. Anderson, V. Suresh, and J. B. Grotberg, "Effect of gravity on liquid plug transport through an airway bifurcation model," J. Biomech. Eng. **127**, 798 (2005).
[48]Y. Zheng, H. Fujioka, J. C. Grotberg, and J. B. Grotberg, "Effects of inertia and gravity on liquid plug splitting at a bifurcation," J. Biomech. Eng. **128**, 707 (2006).
[49]D. M. Campana, S. Ubal, M. D. Giavdoni, and F. A. Saita, "Stability of the steady motion of a liquid plug in a capillary tube," Ind. Eng. Chem. Res. **46**, 1803 (2007).